The simulation model previously described (*5*) has allowed us to examine various possible explanations for the observed nonexponential charge transfer kinetics in photosynthesis. Most important are correlations in the energy gap that persist beyond 1 ps. The underlying motions are slow enough so that their effects on the charge transfer can be viewed qualitatively in terms of a statistical distribution of thermodynamic driving forces. The distinction between a statistical model and a dynamical treatment can be of importance, however, for quantitative issues. The temperature dependence of the charge transfer kinetics may be one such issue. Lowering temperature will likely increase k_1 and decrease k_2 (because these slopes specify rates for essentially activationless and slightly activated crossings, respectively). Lowering temperature, T, should also decrease x_1 (because the mean squared amplitude of low-frequency fluctuations scales as T). It does not necessarily follow, however, that lowering temperature will cause $S(t)$ to exhibit both a shorter time decay of decreased amplitude and a slower long-time decay of increased amplitude. The dynamically mediated constants, κ_+, κ_-, and χ_+, precisely follow the trends of k_1, k_2, and x_1 only in the statistical or inhomogeneous case (that is, with small values of ν). Outside that regime, the correspondence is not quite so simple, as is evident from Eqs. 5 and 6. The underlying surface-hopping model neglects nuclear tunneling effects that are significant at very low temperatures. Nevertheless, these equations illustrate how the temperature dependence may be more complicated than what might be conceived of from a purely statistical perspective. This particular topic is worthy of future theoretical work, both with molecular dynamics and analytical modeling.

REFERENCES AND NOTES

1. M. H. Vos *et al.*, *Proc. Natl. Acad. Sci. U.S.A.* **88**, 8885 (1991); M. H. Vos, F. Rappaport, J.-C. Lambry, J. Breton, J.-L. Martin, *Nature* **363**, 320 (1993).
2. M. Du *et al.*, *Proc. Natl. Acad. Sci. U.S.A.* **89**, 8517 (1992).
3. P. Hamm *et al.*, *Biochim. Biophys. Acta* **1142**, 99 (1993).
4. M. G. Muller, K. Griebenow, A. R. Holzwarth, *Chem. Phys. Lett.* **199**, 465 (1992).
5. M. Marchi, J. N. Gehlen, D. Chandler, M. Newton, *J. Am. Chem. Soc.* **115**, 4178 (1993).
6. For an equilibrated molecular dynamics run of 60 ps as described (*5*), the coordinates of all the nitrogens in the chromophores at the center of the reaction center were recorded every 2.4 fs. The file of these coordinates and the local electrostatic potentials, nitrogen.dat, can be accessed in the directory, rxncntr, through anonymous Internet file transfer protocol (ftp) from hydrogen.cchem.berkeley.edu.
7. M. A. Thompson and M. C. Zerner, *J. Am. Chem. Soc.* **113**, 8210 (1991).
8. W. W. Parson, Z.-T. Chu, A. Warshel, *Biochim. Biophys. Acta* **1017**, 251 (1990).
9. R. A. Goldstein, L. Takiff, S. G. Boxer, *ibid.* **934**, 253 (1988); A. Ogrodnik, M. Volk, R. Letterer, R. Feick, M. E. Michel-Beyerle, *ibid.* **936**, 361 (1988).
10. G. R. Fleming, J. L. Martin, J. Breton, *Nature* **333**, 190 (1988).
11. One may arrive at the ± 0.5 kcal mol^{-1} uncertainty in ε^* from the simulation averages and statistical uncertainties (*5*), together with the experimental driving force (*9*) and a plausible range for the optical dielectric constant of the proteic system (that is, $\epsilon_\infty = 1.9 \pm 0.3$). Alternatively, this estimate of the uncertainty can be derived by following precisely the analysis described in (*5*) to compute ε^* and asserting a ± 4 kcal mol^{-1} uncertainty in the vacuum redox potentials of Thompson and Zerner (*7*).
12. J. Ulstrup, *Charge Transfer in Condensed Media* (Springer-Verlag, Berlin, 1979).
13. N. G. van Kampen, *Stochastic Processes in Physics and Chemistry* (North-Holland, Amsterdam, 1981), pp. 203–208.
14. Z. Wang, R. M. Pearlstein, Y. Jia, G. R. Fleming, J. R. Norris, *Chem. Phys.* **176**, 421 (1993).
15. Y. Jia *et al.*, *J. Phys. Chem.* **97**, 13180 (1993).
16. A. J. Leggett *et al.*, *Rev. Mod. Phys.* **59**, 1 (1987); U. Weiss, *Quantum Dissipative Systems* (World Scientific, River Edge, NJ, 1993).
17. H. Treutlein *et al.*, *Proc. Natl. Acad. Sci. U.S.A.* **89**, 75 (1992).
18. C. C. Moser, J. M. Keske, K. Warncke, R. S. Farid, P. L. Dutton, *Nature* **355**, 796 (1992).
19. A. Helms, D. Heiler, G. McLendon, *J. Am. Chem. Soc.* **113**, 4325 (1991).
20. G. J. Small, J. M. Hayes, R. J. Silbey, *J. Phys. Chem.* **96**, 7499 (1992); P. A. Lyle, S. V. Kolaczkowski, G. J. Small, *ibid.* **97**, 6924 (1993).

21. Supported by NSF through an allocation at the University of California, San Diego, Super Computer Center and by the Department of Energy through support to D.C. and J.N.G. M.M. has benefited from support and encouragement from G. Ciccotti of Centre Européen de Calcul Atomique et Moleculaire. In addition, communications with G. R. Fleming and J. R. Norris have been helpful.

28 September 1993; accepted 1 December 1993

Decomposition of the Modulated Waves in a Rotating Couette System

Yasushi Takeda,* Walter E. Fischer, Jun Sakakibara

The time-dependent velocity field in a rotating Couette system has been decomposed. Successive instantaneous velocity profiles were obtained by an ultrasonic Doppler velocity profile method, and the spatiotemporal velocity field had been analyzed by two-dimensional Fourier transform. The Fourier spectrum is depicted by intrinsic peaks, and the velocity field cpan be reconstructed with these peak components only, indicating a successful decomposition of the velocity field. This method shows that the so-called broadband component, which is purely spatiotemporal and attributed to chaos, corresponds to a global motion of the wave propagating from roll to roll.

Decomposition of velocity fields in fluid flow into spatial and temporal modes of orthogonal eigenfunctions has long been a challenge in the investigation of hydrodynamic instabilities and coherent structures in turbulence. The theoretical basis has been developed as a proper orthogonal decomposition (or Karhunen-Loeve expansion) (*1*, *2*), an empirical orthogonal decomposition (*3*), a singular value decomposition (*4*), and a bi-orthogonal decomposition (*5*), to name a few. These have been tested primarily with computed flow fields. There have been, however, only few applications to experimental work (*3–8*). This is mainly because of the lack of a suitable measurement method that can obtain spatial information on the velocity field with sufficient data as well as good time resolution. We have developed a method that makes use of a pulsed ultrasonic Doppler technique (*9*). This method allows us to obtain the spatiotemporal information necessary to decompose the velocity field.

Y. Takeda and W. E. Fischer, Paul Scherrer Institute, Villigen, Switzerland.
J. Sakakibara, Department of Mechanical Engineering, Keio University, Yokohama, Japan.

*To whom correspondence should be addressed.

We applied this method to investigate the modulated wavy state of the flow in a rotating concentric double cylinder. This configuration, a rotating Couette system, is frequently used to investigate a passage of flow transition from a laminar state to turbulence because the transition is gradual and has no hysteresis with respect to the Reynolds number (*10*). With this configuration, it was also concluded that the flow goes from a laminar to a chaotic state and eventually displays turbulence (*11*).

In a system with the outer cylinder fixed, the fluid in the annular gap moves as a sheet without an axial velocity component for small Reynolds numbers. The first flow instability sets in at a critical Reynolds number (R_c), resulting in the formation of a roll structure [Taylor vortex flow (TVF)] with a nonzero axial velocity component. The flow configuration then consists of stacked tori (rolls) of a pair of countercirculating vortices. At higher Reynolds numbers, a second instability sets in, and an azimuthal wave appears [wavy vortex flow (WVF)]. Power spectrum studies (*11–13*) of this flow indicate that WVF has a single mode and is periodic. At still higher Reynolds numbers, this azimuthal wave is mod-

ulated by second wave modes [modulated wavy vortex flow (MWV)], and the motion becomes quasi-periodic (*12*, *13*). Both TVF and WVF are well understood with respect to their instabilities and static characteristics (*10*). The MWV, however, has received less attention. This seems to be because of the complexity of the flow field; it is nonlinear in nature and appears as a spatiotemporal variation. Moreover, it is difficult to investigate experimentally. One of the few established facts is its azimuthal wave motion; the single periodic wave is attributed to WVF, and several (likely two) additional waves cause a modulation that leads to MWV (*9*–*16*).

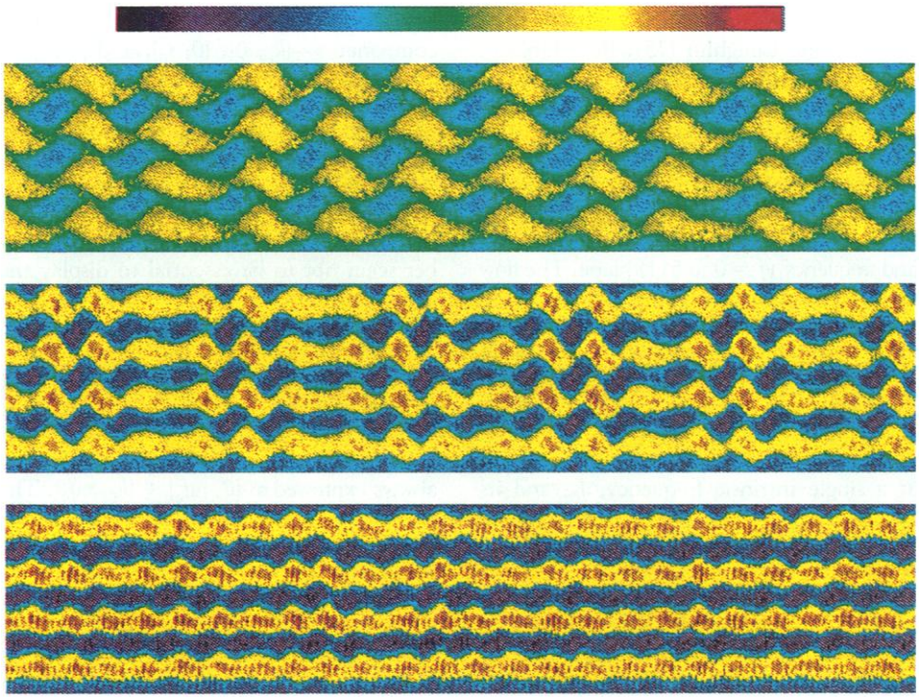

Fig. 1. Measured velocity fields for R^* = 7.07 (top), 13.63 (middle), and 17.92 (bottom). In each display, the ordinate represents position (128 data points for 94 mm in width) and the abscissa is time (1024 points for 135 s). The velocity values are color coded: yellow and red being positive; green and blue, negative. Full scale is ± 36.7 mm/s.

Because the flow field in this configuration has a well-defined spatial and temporal periodicity, the two-dimensional (2D) Fourier spectrum in the wave number and frequency domains is depicted by characteristic peaks corresponding to fundamental wave modes and their harmonics. The velocity field can be reconstructed by these peak components. Through this decomposition, we find that the so-called broadband component observed in the power spectra (*11*) can be attributed to a global motion of waves traveling from roll to roll.

Our Couette system has the following parameters: inner radius, r_i = 94.0 mm; outer radius, r_o = 104.00 mm (radius ratio, η = 0.904); and column length, 200 mm (aspect ratio Γ = 20). Only the inner cylinder is rotated. For the onset of TVF, R_c = 134.5, where the Reynolds number is defined as $R = \Omega r_i d/\nu$ (Ω is the rotational speed, $d = r_o - r_i$ is the gap distance, and ν is the kinematic viscosity). The reduced Reynolds number is $R^* = R/R_c$. The liquid used was a mixture of water and 30% glycerol (*17*–*20*).

We have developed a technique, the ultrasonic Doppler method, for measuring instantaneous velocity profiles. It uses pulsed echography of ultrasound together with the detection of a Doppler shift in frequency. Position information is given by the time lapse between pulse emission and echo reception, and velocity information is obtained from the Doppler shift at each instant, from which an instantaneous velocity profile can be obtained. More detail of the method and the developed system is described elsewhere (*9*). With this method, one can measure a velocity field in the form of 128 data points with a spatial resolution of 0.75 mm (91 mm wide) every 32 to 130 ms (depending on the velocity level). A total of 1024 profiles can be successively recorded.

To take measurements, we fixed an ultrasonic transducer to the outside wall of one of the end plates with the line of

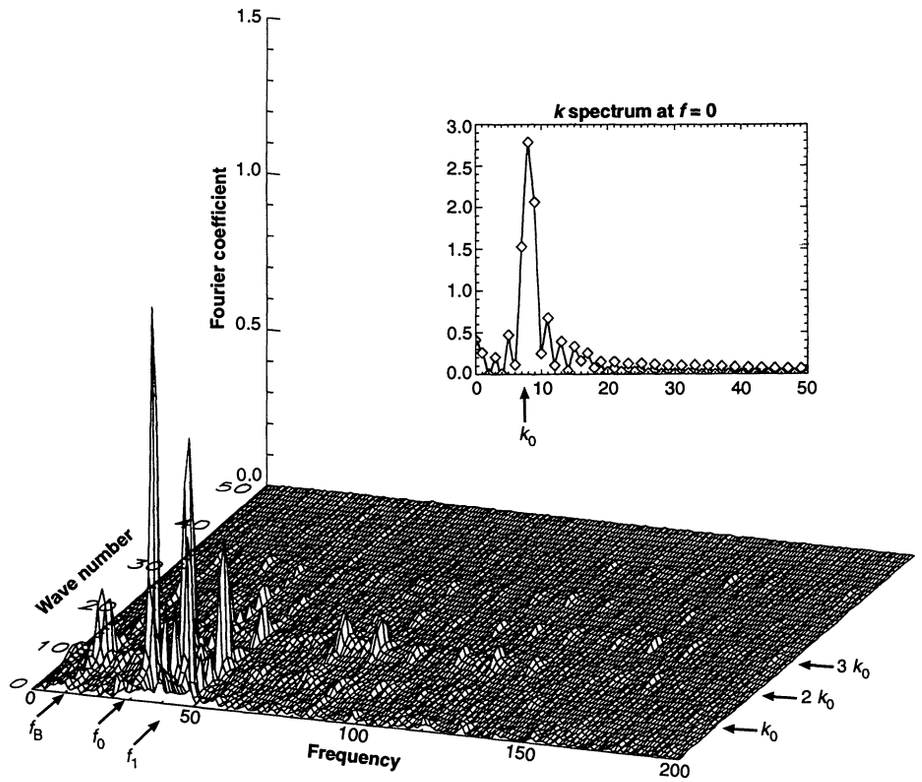

Fig. 2. Two-dimensional Fourier spectrum; the lower portion is shown for clarity. The horizontal axis is frequency (0 to 1.48 Hz with a resolution of 7.4 mHz), and the other axis is the wave number (0 to 0.55 mm^{-1} with a resolution of 0.011 mm^{-1}). Vertical axis is the absolute value of Fourier coefficients ($|S_{ij}|$). (**Inset**) The spectrum at f = 0. The raw velocity field is shown in Fig. 3A.

measurement perpendicular to this plate. The center of the transducer was in line with the inner wall of the outer cylinder. We measured the velocity field of the axial component as a function of axial position and time, $V_z(z, t)$, along the outer wall. Because the diameter of the ultrasound beam is 5 mm, the measurement volume of a data point is shaped like half of a disk with a radius of 2.5 mm and a thickness of 0.75 mm. Only data from the region between 40 (from the end plate) to 135 mm (about four axial wavelengths) was used, to eliminate end effects (*18*, *20*).

Each data set is composed of 128 × 1024 velocity values in matrix form, V_{ij}, where i = 0 to 127 represents the spatial coordinate in the axial direction and j = 0 to 1023 represents the time coordinate. The spatiotemporal nature of the flow field is clearly obtained and displayed on the raw data (Fig. 1). The Fourier transform of this data set in the time domain generates a position-dependent power spectrum. From the space-averaged power spectra, we found that three wave modes (one for WVF and two for MWV) whose frequencies are incommensurate can coexist for a relatively wide range of Reynolds number (*19*). The Fourier transform in the space domain, on the other hand, generates a time-dependent energy spectral density (in the axial direction in the present case) directly as a function of the axial wave number. From the time-averaged energy spectral density, we showed that the energy spectral density is exponential with respect to wave number (*20*), which is supported by the numerical simulations by Marcus (*14*) and Coughlin (*15*). Both kinds of spectra show peak structures corresponding to the spatial and time periodicity of the flow field. They are reported in detail separately in (*19*) and (*20*), respectively.

The same data can be analyzed by a 2D Fourier transform to generate the 2D spectrum on the wave number (k = 0 to 127) and frequency (f = 0 to 511) plane. The flow field can then be characterized by the isolated peaks (designated as $[nk_p, mf_q]$, where n, m, p, and q are integers) (Fig. 2). Peaks are found at the wave number corresponding to the wavelength of a pair of rolls of TVF (k_0 and its higher harmonics nk_0). In the WVF regime (not shown here), we observe peaks at a single intrinsic frequency, f_0, and its harmonics, $[k_0, mf_0]$. In the MWV regime (Fig. 2), two intrinsic frequencies (f_0 and f_1) appear. In all the cases, $[k_0, 0]$ (Fig. 2, inset) corresponds to a TVF existing over a whole range of Reynolds number studied here, and $[0, f_0] + [k_0, f_0]$ (plus sign designates a pair of peaks) corresponds to a pure WVF mode. The case of $[0, f_1] + [k_0, f_1]$ can be attributed to the modulating wave of the MWV mode because this appears only in this regime. Identifying each peak and specifying their combinations, we can reconstruct the velocity field of each mode by making an inverse Fourier transform. For WVF, only the three components—$[k_0, 0]$, $[0, f_0]$, and $[k_0, f_0]$—are needed to reproduce the velocity field quite precisely. As for MWV, five components, with the additional peaks $[0, f_1]$ and $[k_0, f_1]$, reproduce the flow field (Fig. 3). Although dc components such as $[nk_0, 0]$ and $[0, mf_q]$ have to be included, higher harmonics in both frequency and wave number seem not to be essential to display the characteristic features of the flow field. This has proved to be a successful decomposition of the velocity field for the present configuration and enables us to study each wave mode separately.

It is interesting that all the WVF and MWV modes show a peak at k = 0; they are always expressed as $[0, mf_q] + [k_0, mf_q]$. The $[0, mf_q]$ component cannot be neglected. However, a mode that corresponds to the so-called broadband component in the power spectrum (*11*) shows no peak at $[0, f_B]$, where f_B is the frequency of this component. This is a single but broad peak in the kf spectrum, $[k_0, f_B]$, which indicates that this component is purely spatiotemporal. Historically, this broad peak component has been considered to be evidence for a transition of the system from a quasi-periodic to chaotic state, leading to a change of an interpretation about the flow transition to turbulence from the Landau picture to the Newhouse-Rouelle-Takens picture. None of the earlier studies of the power spectrum, however, could resolve this component clearly to distinguish it from quasi-periodic modes.

From the velocity field reconstructed with this component, we found that this mode is associated with a global motion of the wave structure in the system (Fig. 4). The wave propagates from roll to roll. Such a global motion has been observed in the counterrotating Couette system (*21*, *22*), where both inner and outer cylinders rotate, but not in a single rotating system. Because this mode is purely spatiotemporal and is expressed singly as $[k_0, f_B]$, it might not have shown up clearly in any conventional point measurement.

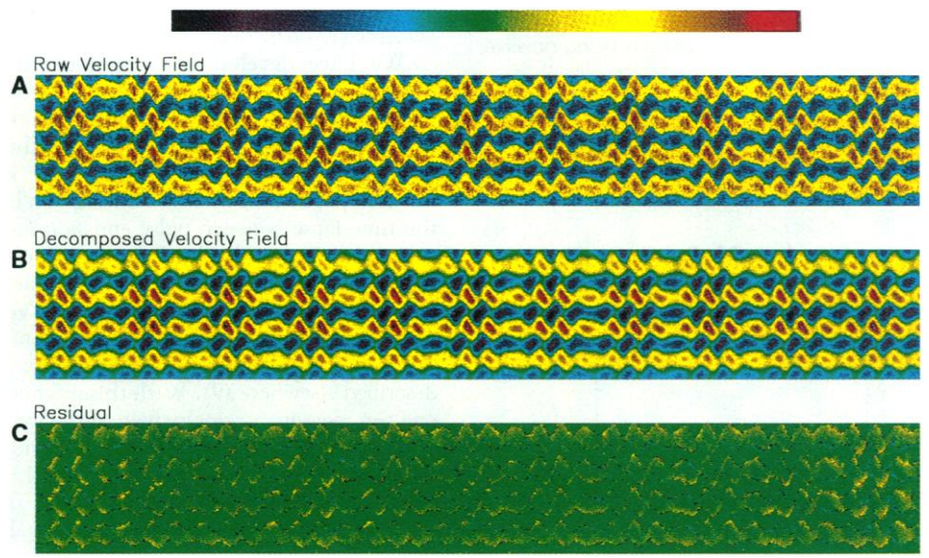

Fig. 3. (**A**) The measured velocity field and (**B**) the reconstructed velocity field. (**C**) A residual between (A) and (B) ($|V_{meas} - V_{dec}|/V_{meas}$, relative scale). For the reconstruction, five components were used: $[k_0, 0]$, $[0, f_0]$, $[k_0, f_0]$, $[0, f_1]$, and $[k_0, f_1]$.

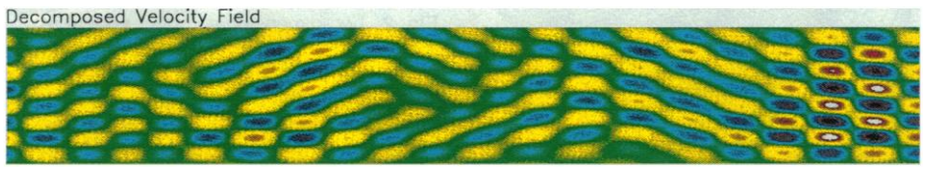

Fig. 4. The decomposed velocity field for the $[k_1, f_B]$ component. The 5 × 5 points on the $[k, f]$ spectrum were used.

REFERENCES

1. J. L. Lumley, in *Atmospheric Turbulence and Radio-Wave Propagation*, A. M. Yaglom and V. I. Tatarski, Eds. (Nauka, Moscow, 1967), pp. 166–178; in *Transition and Turbulence*, R. E. Meyer, Ed. (Academic Press, New York, 1981), pp. 215–242.
2. G. Berkooz, P. Holmes, J. L. Lumley, *Annu. Rev. Fluid Mech.* **25**, 539 (1993).
3. L. Sirovich, in *New Perspectives in Turbulence*, L. Sirovich, Ed. (Springer-Verlag, New York, 1992), pp. 139–163.

4. D. S. Broomhead and G. P. King, *Phys. D* **20**, 217 (1986).
5. M. P. Chauve and P. LeGal, *ibid.* **58**, 407 (1992).
6. J. L. Lumley, in (*3*), pp. 105–122.
7. N. Aubry *et al.*, *J. Fluid Mech.* **192**, 115 (1988).
8. A. Glezer, Z. Kadioglu, A. J. Pearlstein, *Phys. Fluids A* **1**, 1363 (1989).
9. Y. Takeda, *Nucl. Eng. Des.* **126**, 277 (1990).
10. R. C. DiPrima and H. L. Swinney, in *Hydrodynamic Instabilities and the Transition to Turbulence*, H. L. Swinney and J. P. Gollub, Eds. (Springer-Verlag, Berlin, 1985), pp. 139–180.
11. P. R. Fenstermacher, H. L. Swinney, J. P. Gollub, *J. Fluid Mech.* **94**, 103 (1979).
12. M. Gorman and H. L. Swinney, *ibid.* **117**, 123 (1982).
13. L. H. Zhang and H. L. Swinney, *Phys. Rev. A* **31**, 1006 (1985).
14. P. S. Marcus, *J. Fluid Mech.* **146**, 65 (1984).
15. K. T. Coughlin and P. S. Marcus, *ibid.* **234**, 1 (1992); *ibid.*, p. 19.
16. ———, R. P. Tagg, H. L. Swinney, *Phys. Rev. Lett.* **66**, 1161 (1991).
17. Y. Takeda, K. Kobayashi, W. E. Fischer, *Exp. Fluids* **9**, 317 (1990).
18. Y. Takeda, W. E. Fischer, K. Kobayashi, T. Takada, *ibid.* **13**, 199 (1992).
19. Y. Takeda, W. E. Fischer, J. Sakakibara, K. Ohmura, *Phys. Rev. E* **47**, 4130 (1993).
20. Y. Takeda, W. E. Fischer, J. Sakakibara, *Phys. Rev. Lett.* **70**, 3569 (1993).
21. D. Andereck, S. S. Liu, H. L. Swinney, *J. Fluid Mech.* **164**, 155 (1986).
22. R. Tagg *et al.*, *Phys. Rev. A* **39**, 3734 (1989).

3 August 1993; accepted 30 November 1993

Constraints on Transport and Kinetics in Hydrothermal Systems from Zoned Garnet Crystals

Bjørn Jamtveit* and Richard L. Hervig

Zonation of oxygen isotope ratios, fluorine, and rare earth element abundances across garnet crystals from the Permian Oslo Rift reflect temporal variation of the hydrothermal system in which the garnets grew. A sharp rimward decrease in the $^{18}O/^{16}O$ ratio (of 5 per mil) across the interface between aluminum-rich garnet cores and iron-rich rims indicates influx of meteoric fluids to a system initially dominated by magmatic fluids. This influx may record the transition from ductile to brittle deformation of the hydrothermally altered rocks. In contrast, fluorine and light rare earth element concentrations increase at the core-rim interface. These data may reflect enhanced advective transport and notable kinetic control on trace element uptake by the garnets during brittle deformation.

Hydrothermal systems play a key role in the chemical differentiation of the Earth's crust. The understanding of such systems requires integrated studies of active as well as ancient systems. Ancient systems contain the integrated results of hydrothermal activity occurring at depths that are inaccessible to direct observations. The main problem when studying ancient systems is to determine their temporal evolution. Analysis of intracrystalline zonation of hydrothermal minerals may provide a more or less continuous record of the processes taking place during the evolution of ancient hydrothermal systems (*1*). Such data are needed to test and complement results obtained from theoretical models of hydrothermal system dynamics. Here, we present ion microprobe analyses (IMPA) of zoned hydrothermal garnets from the Permian Oslo Rift, Norway, which provide information on the sources of hydrothermal fluids, their compositional evolution, and the extent and mechanism of mass transfer between fluids and the rock matrix.

The garnets that we studied are representative of a large population of hydrothermal garnets from layered shale-carbonate rock sequences in the contact aureole of the Drammen granite (*1*). These rocks were infiltrated by fluids during cooling of the granite. Early infiltration was pervasive and coeval with more or less ductile deformation, whereas later infiltration was focused along faults and fractures formed during brittle deformation (*1*, *2–4*). Garnets grew throughout these events. Mineral equilibria and fluid inclusion results indicate that the garnets formed at temperatures of 350°C to 400°C. Backscattered electron (BSE) images (Fig. 1) show a sharp transition from a relatively grossular-rich core (gr = 20 to 40 mol%) to an andradite-rich rim (gr <5 mol%). The rim furthermore contains several thin layers of more grossular-rich composition that give rise to the oscillatory zonation pattern evident in the BSE image (Fig. 1). The composition of the grossular-rich layers was largely determined by the local mineral assemblage during periods of slow fluid influx and low crystal growth rates, whereas the composition of more rapidly grown (*5*) andradite-rich layers reflects infiltration of externally derived hydrothermal fluids with high concentrations of As and W (*1*, *6*). The andradite-rich garnets are extremely low in high–field strength elements (HFEs) such as Zr, Y, and Ti. The lack of evidence that local sources of HFEs (notably zircon and sphene) were removed from the system indicates that the fluids did not reach equilibrium concentrations with respect to these components during growth of the andradite-rich rims. Thus, models of fluid flow and chemical reaction kinetics in hydrothermal systems that assume local fluid-rock equilibrium may not always be valid (*7*). To obtain more detailed information about the mass transport, mass transfer, kinetic dispersion, aqueous complexation, and the fluid sources, we analyzed the garnet shown in Fig. 1 for oxygen isotope, fluorine, and rare earth element (REE) compositions.

The oxygen isotope zonation profile (Fig. 2A) reveals a marked discontinuity at the core-rim interface, suggesting that the pore fluid had a relatively higher oxygen isotope ratio when the garnet core was growing. Fractionation factors for the garnet-H_2O system at 350°C, corrected for compositional variations of the garnet (*8*, *9*), indicate that the core and rim precipitated from fluids with average $\delta^{18}O$ values [relative to standard mean ocean water (SMOW)] of +10 per mil and +6 per mil, respectively. A value of +10 per mil is that expected for fluid equilibrated with the Drammen granite at high temperature (*4*), whereas the value of +6 per mil may indicate an appreciable meteoric water component in the hydrothermal fluid [the oxygen composition of Permian meteoric water in this area was probably around −12 per mil (*10*)].

Additional information on changes in the hydrothermal system is provided by F and REE data from the garnet. Considerable amounts of F may substitute for OH

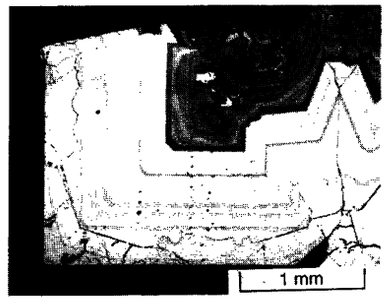

Fig. 1. Backscattered electron image of a dodecahedral garnet crystal selected for ion microprobe analysis. The garnet is essentially a binary solution between the end members grossular (gr = $Ca_3Al_2Si_3O_{12}$) and andradite (and = $Ca_3Fe_2Si_3O_{12}$). The image shows andradite-rich garnet (light color) growing on grossular-richer core (dark). Oscillatory zonation seen in andradite-rich rim reflects different relative proportions of major components andradite and grossular. Dark spots show the sites of oxygen isotope analyses.

B. Jamtveit, Department of Geology, University of Oslo, Post Office Box 1047 Blindern, N-0316 Oslo, Norway.
Richard L. Hervig, Center for Solid State Science, Arizona State University, Tempe, AZ 85287.

*To whom correspondence should be addressed.